JPhys Energy

PURPOSE-LED PUBLISHING™

PAPER • OPEN ACCESS

Processing-structure-property relationships in practical thin solid-electrolyte separators for all-solid-state batteries

To cite this article: Junhao Li *et al* 2024 *J. Phys. Energy* **6** 025023

View the article online for updates and enhancements.

You may also like

- 2024 roadmap for sustainable batteries
Magda Titirici, Patrik Johansson, Maria Crespo Ribadeneyra et al.
- Catalyst integration within the air electrode in secondary Zn-air batteries
Matthew Labbe and Douglas G Ivey
- Advances in sweat-activated batteries for powering wearable electronics: structures, materials, challenges, and perspectives
Yu Yuan, Yile Lu, Tianyue Liang et al.

This content was downloaded from IP address 92.20.177.47 on 15/01/2025 at 13:57

IOP Publishing J. Phys. Energy 6 (2024) 025023 https://doi.org/10.1088/2515-7655/ad3d0b

Journal of Physics: Energy

CrossMark

OPEN ACCESS

RECEIVED
9 February 2024

REVISED
22 March 2024

ACCEPTED FOR PUBLICATION
10 April 2024

PUBLISHED
18 April 2024

Original content from this work may be used under the terms of the Creative Commons Attribution 4.0 licence.

Any further distribution of this work must maintain attribution to the author(s) and the title of the work, journal citation and DOI.

PAPER

Processing-structure-property relationships in practical thin solid-electrolyte separators for all-solid-state batteries

Junhao Li[1,2,6], **Soochan Kim**[1,2,5,6], **Lorenzo Mezzomo**[1,3,6], **Yvonne Chart**[1,2], **Jack Aspinall**[1,2], **Riccardo Ruffo**[3,4] **and Mauro Pasta**[1,2,*]

[1] Department of Materials, University of Oxford, Parks Road, Oxford OX1 3PH, United Kingdom
[2] The Faraday Institution, Quad One, Didcot OX11 0RA, United Kingdom
[3] Dipartimento di Scienza dei Materiali, Università di Milano-Bicocca, via R. Cozzi 55, 20125 Milano, Italy
[4] National Reference Centre for Electrochemical Energy Storage (GISEL)—Consorzio Interuniversitario Nazionale per la Scienza e Tecnologia dei Materiali (INSTM), 50121 Firenze, Italy
[5] School of Chemical Engineering, Sungkyunkwan University, Suwon 16419, Republic of Korea
[6] These authors contributed equally: Junhao Li, Soochan Kim, and Lorenzo Mezzomo.
[*] Author to whom any correspondence should be addressed.

E-mail: mauro.pasta@materials.ox.ac.uk

Keywords: all-solid-state batteries, thin solid-electrolyte separator, processing, practical, Li_6PS_5Cl

Supplementary material for this article is available online

Abstract

Scalable processing of thin and robust solid-electrolyte (SE) separators is key for the commercialization of high-energy all-solid-state batteries (ASSBs). Herein, we report the preparation of Li_6PS_5Cl-based thin SE separators incorporating suitable binders for potential use in ASSBs by two scalable wet processing techniques: tape-casting with nitrile-butadiene rubber (NBR) and calendering with carboxylated nitrile butadiene rubber (XNBR). By means of tensile testing and electrochemical impedance spectroscopy, the influence of processing on the mechanical as well as the electrochemical properties of the resulting thin SE separators is investigated. A trade-off between the mechanical and electrochemical properties is observed, which is due to the inextricably linked microstructures (particle size, binder content and distribution, and porosity) induced by the two different processes. Thin SE separators prepared using the tape-casting method with the more well-distributed binder network demonstrate superior tensile mechanical properties compared to the ones prepared by the calendering method. The results provide insights into the processing-structure-property relationships of the thin SE separators, which will contribute to advancing the application of practical thin solid electrolytes in ASSBs.

1. Introduction

As a promising alternative energy storage technology to conventional Li-ion batteries (LIBs), all-solid-state batteries (ASSBs) have attracted much attention due to their higher energy density and superior safety characteristics [1, 2]. By enabling the reliable use of lithium (Li) metal anodes, ASSBs have the potential to realize improved performance with specific energy > 500 Wh kg^{-1} and energy density > 1500 Wh L^{-1} [3]. To unlock their full potential, replacing a thick pelletized solid-electrolyte (SE) separator with a thin and robust one with the following requirements is key: (1) reducing SE separator thickness to ~ 30 μm while maintaining an acceptable and moderate ionic conductivity to shorten Li-ion transport distance and reduce internal resistance [4–6]; (2) sufficient mechanical strength to resist fracture or Li dendrite penetration over long-term ASSB cycling. However, processing such thin and robust SE separators at the scale required for practical ASSBs is still challenging.

A number of different processing methods have emerged for thin solid-electrolyte (TSE) separators. For example, the commercialized lithium/lithium phosphorus oxynitride (LiPON)/lithium cobalt oxide thin film ASSB contains a 1–2 μm thick amorphous LiPON SE [7]. However, these thin films typically exhibit poor ionic conductivity and are fabricated using vacuum-based deposition methods, such as chemical and

© 2024 The Author(s). Published by IOP Publishing Ltd

physical vapor deposition which are not cost-effective for industrial-scale cell manufacturing [8–10]. Dry processing is also being developed as an alternative, more sustainable technique to produce electrodes and SE separators as it avoids the use of toxic and hazardous solvents [11]. However, this methodology is still at an early stage of development and incompatible with current LIB manufacturing processes. In comparison, by exploiting well-established wet processing methods such as tape-casting or calendering [4, 12–14], flexible TSEs incorporating suitable binders can be continuously fabricated using existing roll-to-roll LIB manufacturing equipments. This will facilitate the faster commercialization of ASSB technology. Although promising, the effect of processing on the properties of the TSE (structural, electrochemical, and mechanical) still requires careful evaluation.

While most work has focused on investigating the ionic conductivity and electrochemical performance of TSEs incorporating suitable binders, there has been minimal focus on understanding their processing-dependent mechanical properties. This is important since the microstructure and mechanical properties of the TSEs can affect the following manufacturing process and the final performance of ASSBs. From a manufacturing perspective, it is vital that the fabricated TSEs are flexible for roll-to-roll manufacturing and malleable for the subsequent mechanically demanding steps like slitting, integrating, and dense packing with cathode and anode layers requiring no high-temperature sintering which may trigger thermal decomposition of the binder. The sulfide electrolyte Li_6PS_5Cl (LPSCl), possessing a relatively high room-temperature ionic conductivity of $\sim$1 mS cm^{-1} and favorable mechanical ductility [15], is a suitable SE for use in TSEs as it can be densified at room temperature. Regarding the performance of ASSBs, the TSEs should have sufficient mechanical strength to withstand prolonged cell cycling without mechanical damage (e.g. fracture or plastic deformation) near the interface due to the stress and strain associated with cyclical volume changes in the electrodes or penetration by Li dendrites.

Consequently, the evaluation of the mechanical properties of different TSEs is essential to develop a complete understanding of these systems. Previous mechanical analysis has mainly focused on bulk SE pellets [16–18], there are few reports for ceramic-rich TSEs. Uniaxial tensile testing is the most common mechanical test and the technique can easily be applied to TSEs due to their high degree of processability and provides a rapid evaluation of important mechanical properties such as tensile modulus. However, only a few research papers have reported the use of tensile testing in the mechanical evaluation of TSEs with a significant or predominant inorganic content due to the difficulty of sample preparation with high ceramic loadings [19–22].

Here, to evaluate the impact of processing on TSEs, we investigate the structural, mechanical, and electrochemical properties of LPSCl-based TSEs prepared using two scalable processing methods: tape-casting with nitrile-butadiene rubber (NBR) and calendering with carboxylated nitrile butadiene rubber (XNBR). These techniques were chosen as tape-casting is known among wet processing methods to be able to produce particularly thin films at high rates and with low surface roughness [23–25]. Calendering is a viable and often preferred alternative to tape-casting as it does not require high-speed and high-energy mixing to prepare the slurry and is up to two to three times faster than tape-casting [26]. The different microstructures (particle size, binder content and distribution, and porosity) that resulted from the two different processes were first examined, and then the corresponding mechanical properties (tensile modulus, tensile strength, and elongation at failure) and ionic conductivity were investigated by means of tensile testing and electrochemical impedance spectroscopy (EIS). A trade-off between the mechanical and electrochemical properties was found and correlated with the processing-dependent microstructures, which will inform research into the optimization of TSEs manufacturing for the mass production of ASSBs.

2. Results and discussion

2.1. Microstructure characterization

As shown in figure 1, the TSE separators were prepared by tape-casting (T) and calendering (C) processes with two binder contents (5 and 10 wt.%) and three densification pressures (0, 100, and 200 MPa) and are denoted as T5/10-0, T5/10-100, and T5/10-200 or C5/10-0, C5/10-100, and C5/10-200, respectively. The TSE with a binder content of 20 wt.% was also prepared and tested, and as it followed the same trends discussed here, the corresponding data are included in the supporting information (SI) for conciseness.

NBR is a commonly used binder for sulfide-based electrolytes. XNBR is a functionalized NBR, characterized by the addition of a polar functional group (–COOH). In addition to their similar chemical structures and comparable tensile moduli (2.15 and 1.55 MPa, respectively) [27, 28], NBR and XNBR were selected due to their solubility in toluene, a nonpolar solvent that has good chemical compatibility with sulfide LPSCl solid electrolyte. Moreover, choosing XNBR for calendering is due to its tendency to form a complex and 'rubbery' composite with LPSCl that enables calendering but prevents tape-casting, whereas NBR is selected for tape-casting because LPSCl and NBR can be mixed in toluene to form a tape-casting

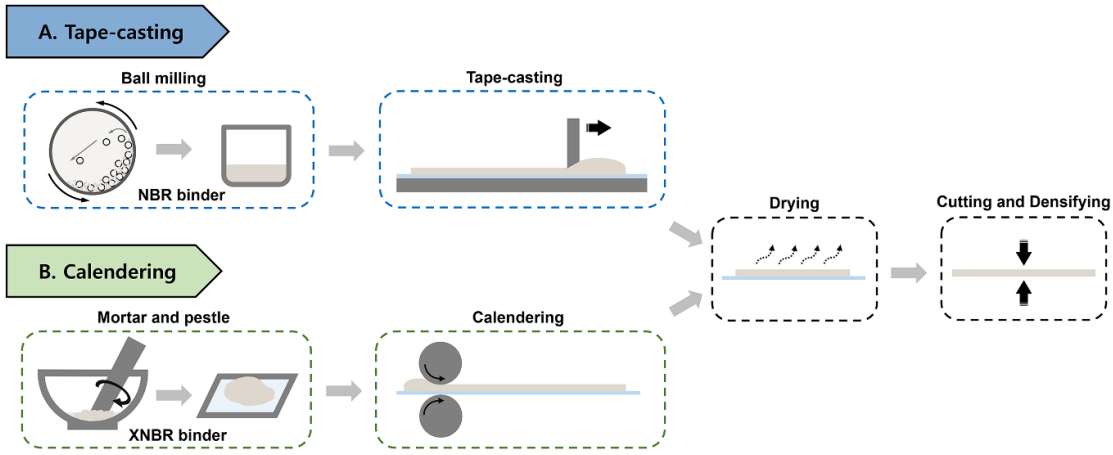

Figure 1. Schematic illustration of the thin solid electrolyte separator fabrication processes (A) tape-casting and (B) calendering. For tape-casting, the Li_6PS_5Cl, NBR, and toluene are mixed by planetary ball milling, and then the prepared slurry is coated on a silicone-coated polyester substrate. For calendering, the Li_6PS_5Cl, XNBR, and toluene are mixed using mortar and pestle, and then the formed 'rubbery' composite is calendered to a free-standing thin separator. After drying at room temperature for 12 h, the obtained thin SE separators by the two processing methods are cut and compressed under a uniaxial press (100 and 200 MPa).

slurry [26]. For the component mixing in the tape-casting process, high-speed and high-energy ball milling is used, which could break down the large LPSCl particles and agglomerates, ensuring the uniform dispersion of materials in the T-TSEs and making it easier to control TSE thickness precisely in the following tape-casting step. Regarding the calendering process, the low-speed and low-energy mechanical mixing could reduce the damage to the LPSCl particles, which in turn decreases the resistance stemming from an increased number of particle interfaces and defects.

Figure 2 shows the influence of the densification on the cross-sectional microstructure of the samples with 5 wt.% binder content characterized by focused ion beam-scanning electron microscopy (FIB-SEM) and the corresponding porosities for the samples with both 5 and 10 wt.% binder contents.

Compared to the pristine powder (figure S1), the LPSCl particles in C-TSEs maintain a similar morphology (figures 2(D)–(F)), with small particles < 3 μm in size and larger particles/agglomerates reaching sizes of 10 μm or more. However, the ball milling step for T-TSEs appears to have broken up these large LPSCl particles/agglomerates, resulting in a different morphology (figures 2(A)–(C)) with reduced particle size and an average particle size of $\leqslant 2$ μm. The reduction in size of the LPSCl particles can be mainly attributed to the high-energy mechanical mixing step involved in the slurry processing and partially due to the NBR binder functioning as a surfactant [12]. The packing of the LPSCl particles becomes much denser as the densification pressure increases. Figures 2(A) and (D) show loosely packed LPSCl particles with an interconnected open-pore network in the pristine T- and C-TSEs. After densification at 200 MPa, only isolated voids are left and parts of the LPSCl particles underwent plastic deformation to some extent that allowed them to aggregate into larger domains with indistinct boundaries between them (figures 2(C) and (F)).

As shown in figures 2(G) and (H), an increase in binder content or densification pressure leads to a reduction in porosity. The porosity of the TSEs with 10 wt.% binder is lower than the one with 5 wt.% binder at the same densification pressure, more significant for C-TSEs, as the binder can fill the voids between the particles. For the T-TSEs, the reduction in porosity with densification appears to follow an approximately linear trend from 0 to 200 MPa, however, this is not the case for the C-TSEs. Notably, there is a more pronounced reduction in porosity when going from C5-100 to C5-200 compared to that from C5-0 to C5-100, as well as going from C10-0 to C10-100. The above observation could be attributed to the more homogeneous microstructure in the T-TSEs compared to the C-TSEs, resulting in a more consistent and uniform densification process. Although a higher degree of densification (> 200 MPa) is expected to result in lower porosity and higher ionic conductivity [12], the resulting TSEs proved too brittle to allow meaningful tensile tests. This brittleness renders such high densification pressures undesirable for our investigation aimed at linking processing, microstructure, and the mechanical and electrochemical properties. Therefore, higher densification pressures are beyond the scope of this work.

The above results of the densification effect on porosity suggest a more homogeneous distribution of binder in the T-TSEs than the C-TSEs. Further, energy-dispersive x-ray spectroscopy (EDX) was performed on the T- and C-TSEs with 5 wt.% binder content after densification at 200 MPa (figures 3(A) and (B)). The sulfur and carbon signals were used to identify the LPSCl and the binder locations, respectively. The

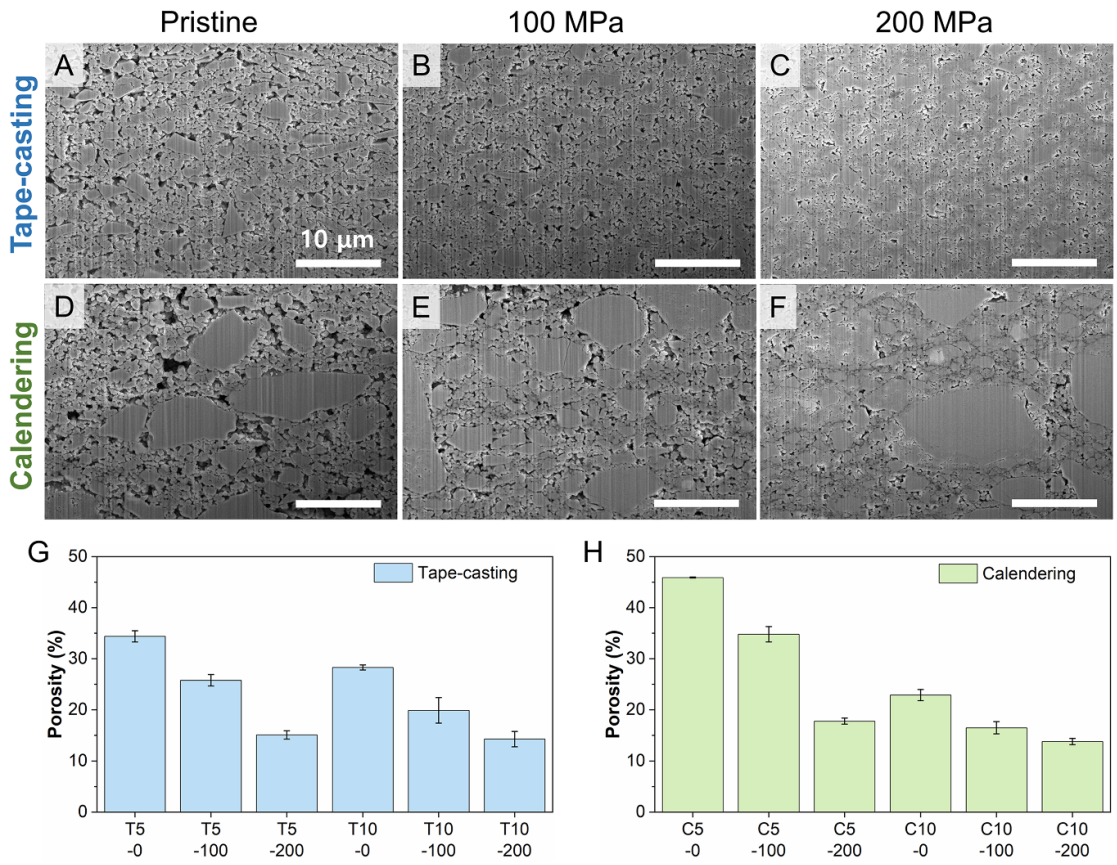

Figure 2. Cross-sectional SEM images of thin solid-electrolyte separators with 5 wt.% binder content prepared by (A)–(C) tape-casting and (D)–(F) calendering processes as a function of densification pressure (A) and (D) pristine, (B) and (E) 100 MPa and (C) and (F) 200 MPa. All the scale bars are 10 μm. Porosity of the thin solid electrolyte separators prepared by (G) tape-casting (T) and (H) calendering (C) processes as a function of densification pressure (0, 100, and 200 MPa denoted by X-0, X-100, and X-200, respectively) and binder content (5 or 10 wt.% denoted by X5 or X10, respectively).

relatively homogeneous sulfur signal in both is as expected. The carbon distribution map gives a qualitative indication that the NBR binder within the T-TSEs is homogeneously wrapping the LPSCl particles, whereas in the C-TSEs the higher intensity of carbon signal in certain areas demonstrates random distribution or agglomeration of XNBR binder at the boundaries of LPSCl particles. This provides further evidence of the more homogeneous microstructure of the T-TSEs in terms of both particle size and binder distribution.

2.2. Mechanical properties

Tensile testing is carried out under Ar atmosphere to understand the mechanical properties of the T- and C-TSEs. The recorded stress-strain curves for the corresponding T- and C-TSEs with different binder contents (5 and 10 wt.%) and densification pressures (0, 100, and 200 MPa) are shown in figures 4(A) and (B). There is a clear difference between the T- and C-TSEs. The stress-strain curves of T-TSEs present a steep linear-elastic region followed by a plateau in which the plastic elongation of the T-TSEs takes place. In comparison, the stress–strain curves of C-TSEs have a very different shape without clear yield points or elongation plateau.

For a quantified comparison, the tensile modulus and ultimate tensile strength (UTS) were determined from the stress-strain curves. For all the samples under investigation, the UTS was defined as the maximum stress before failure. Figures 4(C) and (D) show the tensile moduli of the tested samples. At the same binder content and densification pressure, T-TSEs with the more well-distributed binder network demonstrate a higher tensile modulus compared to the counterparts prepared by the calendering method with the binder partially covering LPSCl particles. Despite the porosities of the T5-200 and C5-200 or T10-200 and C10-200 samples are comparable, the tensile modulus of the T-TSEs is nearly twice that of the C-TSEs. Both T- and C-TSEs displayed an obvious increase in tensile modulus upon densification for both binder contents. For pristine TSEs higher tensile modulus values are observed with higher binder loadings, however, this effect is reversed after densification. The tensile modulus of the T5-200 and C5-200 are approximately double the values for their 10 wt.% counterparts.

Figures 4(E) and (F) show the UTS and elongation at failure of the tested samples. For T-TSEs, as the densification pressure increases, the UTS increases whereas the elongation at failure decreases. The binder

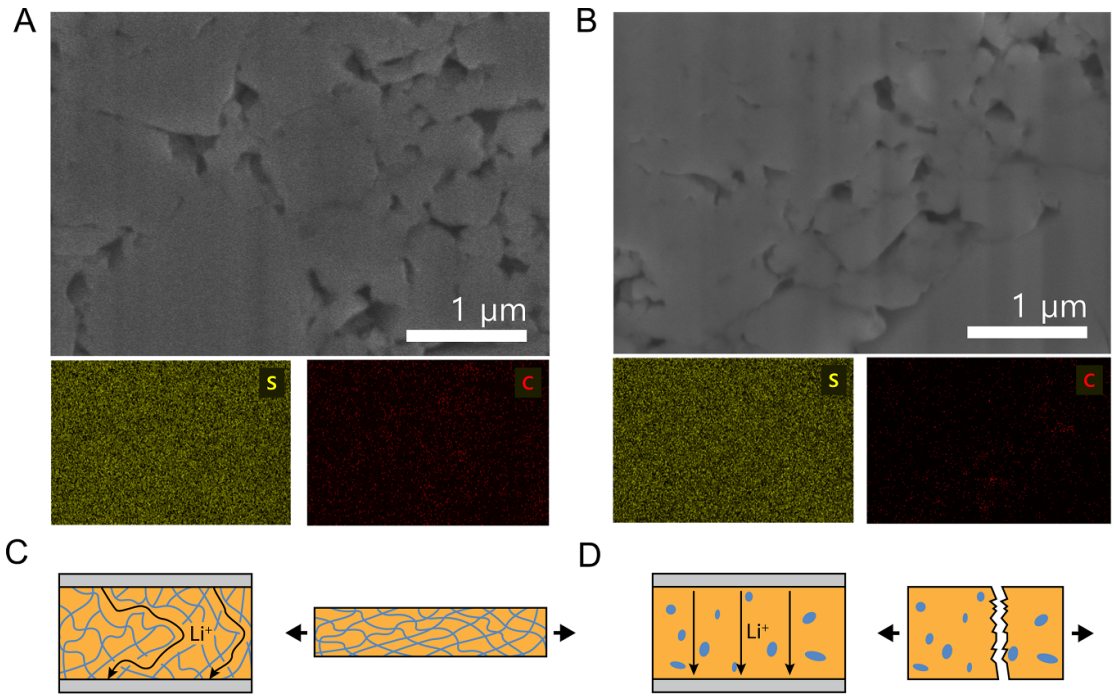

Figure 3. Magnified cross-sectional SEM images and EDX mapping results of polymer binder distribution in thin solid-electrolyte separators with 5 wt.% binder content prepared by (A) tape-casting and (B) calendering processes. Schematic illustration of the structures of the thin solid-electrolyte separators prepared by (C) tape-casting and (D) calendering processes along with the trade-off relationship between the mechanical and electrochemical properties.

content has a significant impact on the UTS and elongation at failure of the densified samples, with the elongation at failure more than doubling when going from 5 to 10 wt.% binder content for both the 100 and 200 MPa densified samples. For C-TSEs, the change in both UTS and elongation at failure with the densification and binder content is much less pronounced. Interestingly, the UTS of T- and C-TSEs are comparable to or higher than the reported values for dry-processed LPSCl-based SEs with a fibrous PTFE binder which possesses a significantly higher tensile strength than NBR or XNBR [21, 29, 30].

The above differences between the T- and C-TSEs could be due to the difference in the LPSCl particle size and binder distribution induced by processing. It has been shown in the literature that the difference in tensile modulus of ceramic-polymer composites is independent of the particle size, but rather depends on the adhesion between the two phases present and stress transfer between phases [31–33]. Therefore, the binder distribution must play the dominant role. As shown in figures 3(C) and (D), a more homogeneous distribution of binder surrounding the smaller LPSCl particles in the T-TSEs enables a more efficient transfer of local stresses between the LPSCl and binder, enhanced by the high adhesion between NBR and sulfide particles [32], which accounts for the higher tensile modulus, UTS, and failure strain in these systems. In comparison, the larger LPSCl particles and less well-dispersed XNBR binder in C-TSEs result in a reduced area for adhesion between the binder and LPSCl particles, leading to lower strain to failure, UTS, and tensile modulus.

From the above, it can be found that the difference in mechanical properties is strongly correlated with the microstructure achieved after the processing and densification. The change in microstructure due to densification significantly influences the mechanical properties in both the T- and C-TSEs, rendering them stiffer and less deformable. At the same binder content and densification pressure, it seems that the mechanical properties are more dependent on the binder distribution.

2.3. Electrochemical properties

Lithium-ion conductivity is the other important property of a TSE. To evaluate this, EIS was performed using custom SSB testing cells under practical operating conditions (stack pressure of 2.5 MPa, 298 K). Figures 5(A) and (B) show the ionic conductivities of the T- and C-TSEs with different binder contents (5 and 10 wt.%) and densification pressures (0, 100, and 200 MPa).

TSEs prepared using both processing methods were found to show improved ionic conductivities with lower binder contents and higher densification pressures. As the binder is non-ionically conductive and would cover parts of the LPSCl particles, a higher proportion of it would reduce the overall conductivity of

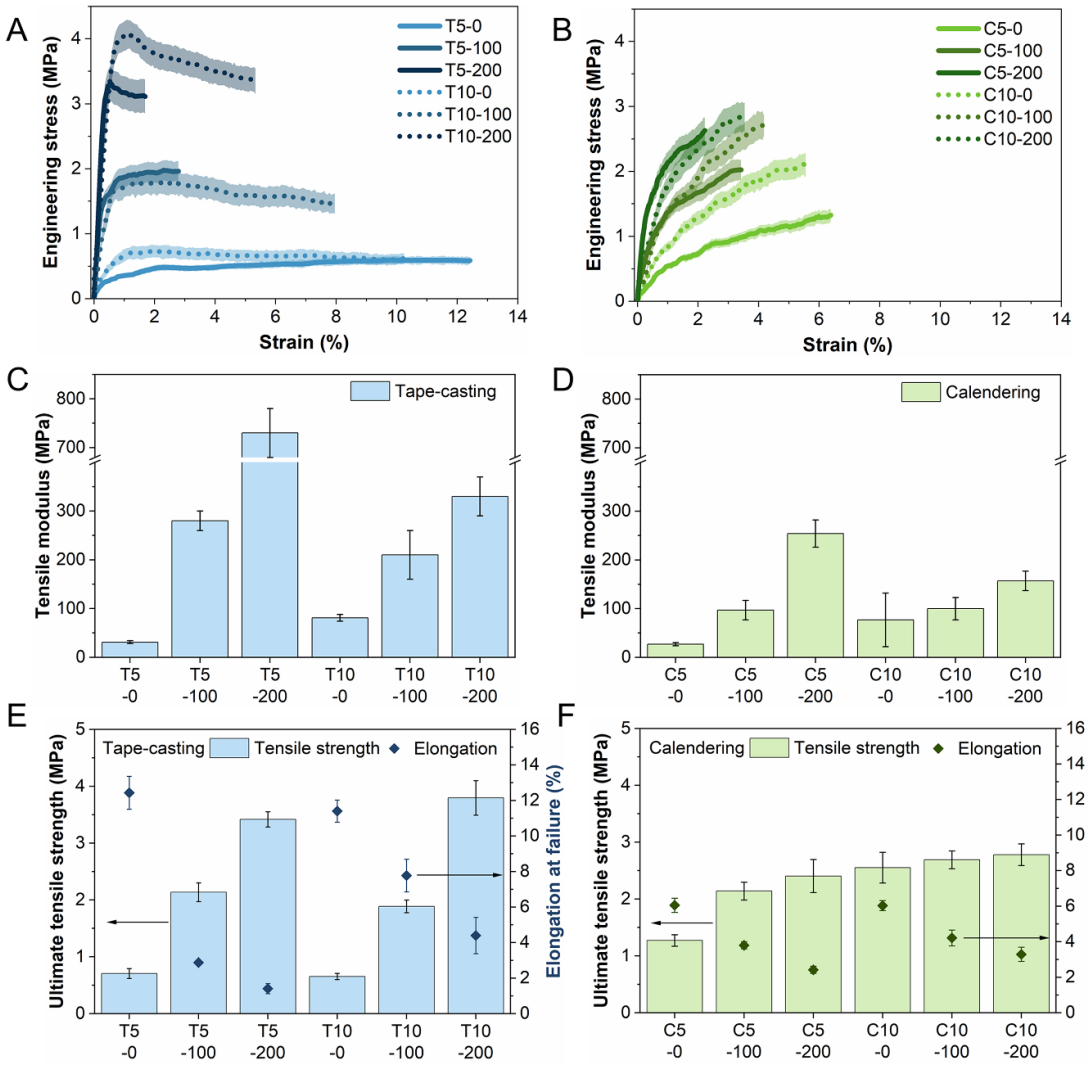

Figure 4. (A) and (B) Representative stress-strain profiles, (C) and (D) tensile modulus, (E) and (F) ultimate tensile strength and elongation at failure of the thin solid-electrolyte separators prepared by (A), (C) and (E) tape-casting (T) and (B), (D) and (F) calendering (C) processes as a function of densification pressure (0, 100, and 200 MPa denoted by X-0, X-100, and X-200, respectively) and binder content (5 or 10 wt.% denoted by X5 or X10, respectively). Error bars are presented as shaded areas around the curves.

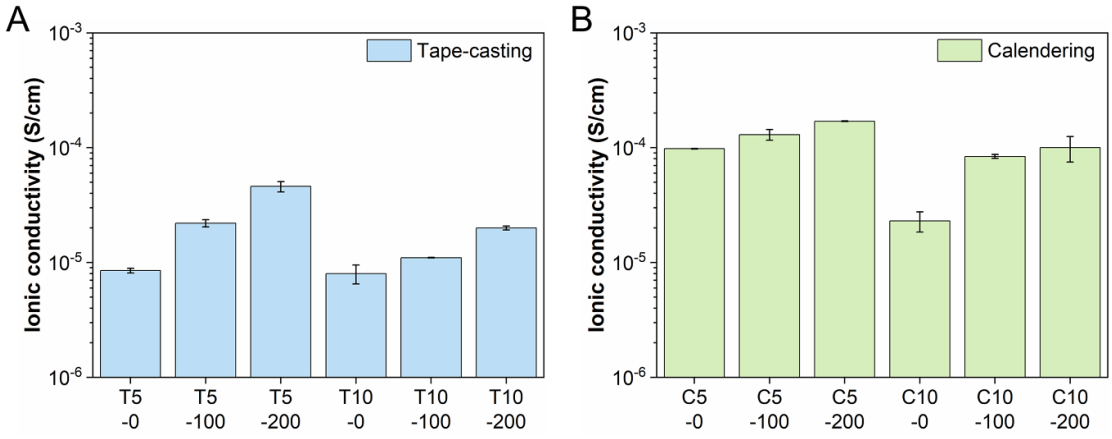

Figure 5. Ionic conductivity of the thin solid-electrolyte separators prepared by (A) tape-casting (T) and (B) calendering (C) processes as a function of densification pressure (0, 100, and 200 MPa denoted by X-0, X-100, and X-200, respectively) and binder content (5 or 10 wt.% denoted by X5 or X10, respectively) measured by electrochemical impedance spectroscopy (EIS) under 2.5 MPa operating pressure.

the TSEs while also reducing the effective contact area between the LPSCl particles and increasing the tortuosity of the Li^+ pathways [34]. On the other hand, the higher ionic conductivities with higher densification pressures arise from the reduced porosity, creating more ion-transport pathways and reducing the tortuosity across the TSEs.

Comparing the two processing methods, C-TSEs have significantly higher ionic conductivities. T-TSEs all show ionic conductivities below 10^{-4} S cm^{-1} with the highest coming from the T5-200 sample (4.6×10^{-5} S cm^{-1}), whereas ionic conductivities close to 10^{-4} S cm^{-1} are obtained for C-TSEs with the highest one coming from the C5-200 sample (1.7×10^{-4} S cm^{-1}). As we use a practical stack pressure of 2.5 MPa, the obtained ionic conductivities are lower than the theoretical value of LPSCl ($\sim 1.0 \times 10^{-3}$ S cm^{-1}) and some other reported values for similar systems, which are usually measured using impractical stack pressures (e.g. $>$ 20 MPa) [34].

Additionally, the ionic conductivities of the C-TSEs are less sensitive to the densification pressure increase than the counterparts of T-TSEs. Specifically, although the porosities of T-TSEs (T5-0, T5-100, and T5-200) are lower than C-TSEs (C5-0, C5-100, and C5-200), the ionic conductivities of C-TSEs are much higher, indicating other factors apart from porosity are the key. The higher ionic conductivities of the C-TSEs can be explained by the following: with the short mixing step in the calendering method, the LPSCl particles were subjected to much less time of the interaction between toluene and LPSCl, which has been observed to have a detrimental effect on the total ionic conductivity of LPSCl powders [35]. Without the high-energy mechanical mixing step used in the tape-casting method, larger LPSCl particles remained in the C-TSEs, which provide longer uninterrupted ion-transport pathways and less interfacial resistance between particles. The XNBR binder in the C-TSEs also tends to randomly distribute at the boundaries of LPSCl particles but does not form a thin insulating layer around the particles, providing fewer barriers and more continuous ion-transport pathways (figure 3(D)). From the above, it is found that the difference in conductivity is not only a function of the binder content but also relies on the SE particle size and binder distribution.

3. Conclusions

In summary, we have compared two practical processing methods which can be used to manufacture TSE separators. The processing of the LPSCl/binder composite has a clear impact on both the mechanical and electrochemical properties of the TSEs, with various microstructural features including particle size, binder content and distribution, and porosity (densification pressure) all playing important roles. TSEs prepared using the tape-casting method yield overall lower ionic conductivities but demonstrate superior tensile mechanical properties, including tensile modulus, tensile strength, and elongation at failure due to the more well-distributed but non-ionically conductive binder network, compared to TSEs prepared by the calendering method. In contrast, TSEs using the calendering method show much higher ionic conductivities but compromised tensile mechanical properties due to the remaining binder partially covering large LPSCl particles with longer undisturbed ionic pathways. The calendered TSE with 5 wt.% XNBR binder densified to 200 MPa is presented as a potential compromise between having an adequately high ionic conductivity for low internal resistance of the ASSB and acceptable mechanical properties for practical use of the separators. This work demonstrates the importance of understanding the processing-structure-property relationships in TSEs, which need further investigation to facilitate the practical manufacture and application of thin SEs.

4. Experimental methods

4.1. Materials

Li_6PS_5Cl (LPSCl) SE powder (99.9%, $\sim$10 μm, Ampcera Inc., density: 1.64 g cm^{-3}), nitrile butadiene rubber (NBR, Krynac 3345F, Arlanxeo, density: 0.97 g cm^{-3}), carboxylated nitrile butadiene rubber (XNBR, Krynac X750, Arlanxeo, density: 0.98 g cm^{-3}) and anhydrous toluene (99.8%, Sigma Aldrich).

4.2. TSE separators preparation

For tape-casting TSEs, the slurries with three compositions (LPSCl and NBR at a weight ratio of 95:5, 90:10, and 80:20) were prepared. Firstly, 500 mg of NBR polymer was fully dissolved in 10 ml of anhydrous toluene. To prepare the slurry, LPSCl was weighed into a ball milling jar before the polymer solution was added. After ball milling for 30 min at 600 rpm in a planetary ball mill (Fritsch Pulverisette 7), the slurry was then coated on a silicone-coated polyester film using the doctor blade technique. After drying at room temperature for 12 h, the TSE was peeled off the substrate, cut, and compressed with stainless steel plungers (10 mm diameter) under a uniaxial press (100 and 200 MPa). The thickness of TSEs with 5 wt.% binder as a function of densification pressure (0, 100, and 200 MPa) is 117 $\pm$ 8, 113 $\pm$ 7, and 80 $\pm$ 5 μm respectively. The thickness of TSEs with 10 wt.% binder as a function of densification pressure (0, 100, and 200 MPa) is

82 ± 6, 75 ± 2, and 64 ± 3 μm respectively. All processes were carried out in an Ar-filled glove box (MBRAUN, MB 200B, $H_2O < 0.1$ ppm, $O_2 < 0.1$ ppm).

Calendered TSEs were prepared by previously reported procedures [26]. LPSCl powder and XNBR binder (5, 10 and 20 wt.%) were combined in anhydrous toluene and mixed using agate mortar and pestle or a vortex mixer for 3 min. The composite was placed between silicone-coated polyester films and calendered to a free-standing thin film. The thickness of the prepared TSE was controlled by setting the gap distance of the calendering machine's rollers (MTI Corp., MSK-2150). After drying at room temperature for 12 h, the TSE was cut and compressed with stainless steel plungers (10 mm diameter) under a uniaxial press (100 and 200 MPa). The thickness of TSEs with 5 wt.% binder as a function of densification pressure (0, 100, and 200 MPa) is 111 ± 11, 93 ± 9, and 97 ± 7 μm respectively. The thickness of TSEs with 10 wt.% binder as a function of densification pressure (0, 100, and 200 MPa) is 100 ± 15, 93 ± 3, and 70 ± 9 μm respectively. All processes were carried out in an Ar-filled glove box (MBRAUN, MB 200B, $H_2O < 0.1$ ppm, $O_2 < 0.1$ ppm).

4.3. Characterization

Porosity of the TSEs was determined using equation (1). Samples of the TSE were punched (10 mm diameter) and their weight (Sartorius Cubis II Ultra Micro Balance) and thickness (Mitutoyo, 293–344 External Micrometer) were measured. W_{TSE} and V_{TSE} are the weight and volume of the TSEs, respectively. χ_a and ρ_a are the weight fraction and density of component a in the composite [26],

$$\varepsilon\,(\text{porosity},\%) = 100 \times \left[1 - (W_{TSE}/V_{TSE}) \times \left(\chi_{LPSCl}/\rho_{LPSCl} + \chi_{polymer}/\rho_{polymer}\right)\right]. \quad (1)$$

Tensile testing was performed using a DEBEN Microtest tensile, compression and horizontal bending stage (MT5000 Dual Leadscrew Tensile Tester H-550 Controller) equipped with a 1 kN load cell operating at 50× gain and with a digital extensometer. Experiments were visually monitored and recorded using a digital camera connected to the ThorCam software. Rectangular-shaped TSE specimens of fixed width and length (0.8 × 3.0 cm) were punched using a die cutter. Their thickness was individually evaluated using a digital screw micrometer gauge with 0.001 mm sensitivity and averaged from three different locations of the specimen. Carefully aligned TSEs were monotonically loaded in tension (extension rate = 1.0 mm min^{-1}) while measuring the resulting force until rupture occurred. At least three specimens were tested for each composition to achieve statistical validation. All the handling and analyses have been carried out in an Ar-filled glove box ($H_2O < 0.1$ ppm, $O_2 < 0.1$ ppm) to avoid any possible degradation of the TSEs. Error bars on the stress-strain curves were computed as a relative error considering the average fluctuations in the force recorded by the DEBEN stage to account for the instrumental sensitivity in the employed force range.

Ionic conductivity of the SE (circular disk, 10 mm diameter) was measured by EIS using a VMP-3 potentiostat (Biologic, France) with a voltage amplitude of 10 mV in the frequency range of 1 MHz to 0.01 Hz with the cell-configuration (carbon-coated Al foil/SE/carbon-coated Al foil). The measurement was carried out using a custom-made battery testing cell under a stack pressure of ∼2.5 MPa at 298 K.

Microstructure characterization of the TSE was carried out using plasma focused ion beam scanning electron microscopy (PFIB-SEM) sectioning. PFIB sectioning was performed using a Thermo Fisher Helios G4-CXe Plasma-FIB. The samples were transferred to the PFIB using an airless transfer vessel (Gatan), then milled and polished using a constant voltage of 30 kV and a current down to 15 nA.

Data availability statement

All data that support the findings of this study are included within the article (and any supplementary files).

Acknowledgments

This work was supported by the Faraday Institution LiSTAR (Grant No. FIRG014) and SOLBAT (Grant No. FIRG026) programs and the Henry Royce Institute (through UK Engineering and Physical Science Research Council Grant No. EP/R010145/1) for capital equipment. The authors are grateful to Arlanxeo for providing the NBR and XNBR samples. Moreover, the authors express gratitude to Ed Darnbrough and Camilla Hurst for their contributions to optimizing the experimental setup for tensile testing.

Author contributions

Junhao Li, Lorenzo Mezzomo, and Soochan Kim: conceptualization, methodology, investigation, writing (original draft), reviewing, and editing. Yvonne Chart: writing, second draft, reviewing, and editing. Jack Aspinall: writing, reviewing, and editing. Riccardo Ruffo: conceptualization, methodology, writing, reviewing and editing, supervision, project administration, and funding acquisition. Mauro Pasta:

conceptualization, methodology, writing, reviewing and editing, supervision, project administration, and funding acquisition.

Conflict of interest

The authors declare no competing interests.

ORCID iDs

Junhao Li https://orcid.org/0009-0004-0526-0730
Lorenzo Mezzomo https://orcid.org/0000-0002-1863-8753
Yvonne Chart https://orcid.org/0000-0003-0523-8627
Jack Aspinall https://orcid.org/0000-0002-6470-3915
Mauro Pasta https://orcid.org/0000-0002-2613-4555

References

[1] Janek J and Zeier W G 2016 A solid future for battery development *Nat. Energy* **1** 16141
[2] Famprikis T, Canepa P, Dawson J A, Islam M S and Masquelier C 2019 Fundamentals of inorganic solid-state electrolytes for batteries *Nat. Mater.* **18** 1278–91
[3] Albertus P *et al* 2021 Challenges for and pathways toward Li-metal-based all-solid-state batteries *ACS Energy Lett.* **6** 1399–404
[4] Wu J, Yuan L, Zhang W, Li Z, Xie X and Huang Y 2021 Reducing the thickness of solid-state electrolyte membranes for high-energy lithium batteries *Energy Environ. Sci.* **14** 12–36
[5] Randau S *et al* 2020 Benchmarking the performance of all-solid-state lithium batteries *Nat. Energy* **5** 259–70
[6] Tan D H, Meng Y S and Jang J 2022 Scaling up high-energy-density sulfidic solid-state batteries: a lab-to-pilot perspective *Joule* **6** 1755–69
[7] Wang B, Bates J B, Hart F X, Sales B C, Zuhr R A and Robertson J D 1996 Characterization of thin-film rechargeable lithium batteries with lithium cobalt oxide cathodes *J. Electrochem. Soc.* **143** 3203–13
[8] Balaish M *et al* 2021 Processing thin but robust electrolytes for solid-state batteries *Nat. Energy* **6** 227–39
[9] Pasta M *et al* 2020 2020 roadmap on solid-state batteries *J. Phys. Energy* **2** 032008
[10] Maclaughlin C M 2019 Innovations in lithium ion battery technologies: a conversation with Will West, Nancy Dudney, and Andrew Westover *ACS Energy Lett.* **4** 786–8
[11] Lu Y, Zhao C-Z, Yuan H, Hu J-K, Huang J-Q and Zhang Q 2022 Dry electrode technology, the rising star in solid-state battery industrialization *Matter* **5** 876–98
[12] Sedlmeier C, Kutsch T, Schuster R, Hartmann L, Bublitz R, Tominac M, Bohn M and Gasteiger H A 2022 From powder to sheets: a comparative electrolyte study for slurry-based processed solid electrolyte/binder-sheets as separators in all-solid-state batteries *J. Electrochem. Soc.* **169** 070508
[13] Parejiya A, Dixit M B, Parikh D, Amin R, Essehli R, Li J, Wood D L and Belharouak I 2022 Understanding slurry formulations to guide solution-processing of solid electrolytes *J. Power Sources* **544** 231894
[14] Schnell J, Günther T, Knoche T, Vieider C, Köhler L, Just A, Keller M, Passerini S and Reinhart G 2018 All-solid-state lithium-ion and lithium metal batteries-paving the way to large-scale production *J. Power Sources* **382** 160–75
[15] Ning Z *et al* 2021 Visualizing plating-induced cracking in lithium-anode solid-electrolyte cells *Nat. Mater.* **20** 1121–9
[16] Baranowski L L, Heveran C M, Ferguson V L and Stoldt C R 2016 Multi-scale mechanical behavior of the Li_3PS_4 solid-phase electrolyte *ACS Appl. Mater. Interfaces* **8** 29573–9
[17] Athanasiou C E *et al* 2022 Rate-dependent deformation of amorphous sulfide glass electrolytes for solid-state batteries *Cell Rep. Phys. Sci.* **3** 100845
[18] Kato A, Yamamoto M, Sakuda A, Hayashi A and Tatsumisago M 2018 Mechanical properties of Li_2S-P_2S_5 glasses with lithium halides and application in all-solid-state batteries *ACS Appl. Energy Mater.* **1** 1002–7
[19] Mezzomo L *et al* 2022 Unveiling the role of PEO-capped TiO_2 nanofiller in stabilizing the anode interface in lithium metal batteries *Nano Lett.* **22** 8509–18
[20] Pan P, Zhang M, Cheng Z, Jiang L, Mao J, Ni C, Chen Q, Zeng Y, Hu Y and Fu K (K) 2022 Garnet ceramic fabric-reinforced flexible composite solid electrolyte derived from silk template for safe and long-term stable all-solid-state lithium metal batteries *Energy Storage Mater.* **47** 279–87
[21] Lee D J *et al* 2023 Physio-electrochemically durable dry-processed solid-state electrolyte films for all-solid-state batteries *Adv. Funct. Mater.* **33** 2301341
[22] Hegde G S and Sundara R 2022 A flexible, ceramic-rich solid electrolyte for room-temperature sodium-sulfur batteries *Chem. Commun.* **58** 8794–7
[23] Emanuel Ximim Gavim A, de Oliveira Mascarenhas R, Selzler Sbrissia L, Valter Barbosas Júnior J, Reges Casagrande T and Gerniski Macedo A 2023 Identifying the manufacturing process of PVC films by nondestructive morphological analyses *Mater. Lett.* **338** 134065
[24] Emley B, Liang Y, Chen R, Wu C, Pan M, Fan Z and Yao Y 2021 On the quality of tape-cast thin films of sulfide electrolytes for solid-state batteries *Mater. Today Phys.* **18** 100397
[25] Singer C, Schmalzbauer S and Daub R 2023 Influence of the slurry composition on thin-film components for the wet coating process of sulfide-based all-solid-state batteries *J. Energy Storage* **68** 107703
[26] Kim S, Chart Y A, Narayanan S and Pasta M 2022 Thin solid electrolyte separators for solid-state lithium-sulfur batteries *Nano Lett.* **22** 10176–83
[27] Vinayasree S, Soloman M A, Sunny V, Mohanan P, Kurian P and Anantharaman M R 2013 A microwave absorber based on strontium ferrite-carbon black-nitrile rubber for S and X-band applications *Compos. Sci. Technol.* **82** 69–75
[28] Manna R and Srivastava S K 2017 Fabrication of functionalized graphene filled carboxylated nitrile rubber nanocomposites as flexible dielectric materials *Mater. Chem. Front.* **1** 780–8

[29] Nasir M, Poh B T and Ng P S 1988 Effect of γ-mercaptopropyltrimethoxysilane coupling agent on t_{90}, tensile strength and tear strength of silica-filled NR, NBR and SBR vulcanizates *Eur. Polym. J.* **24** 961–5
[30] Fischer S and Brown N 1973 Deformation of polytetrafluoroethylene from 78 to 298 K and the effects of environmental crazing *J. Appl. Phys.* **44** 4322–7
[31] Fu S Y, Feng X Q, Lauke B and Mai Y W 2008 Effects of particle size, particle/matrix interface adhesion and particle loading on mechanical properties of particulate-polymer composites *Composites* B **39** 933–61
[32] Vollenberg P H and Heikens D 1989 Particle size dependence of the Young's modulus of filled polymers: 1. Preliminary experiments *Polymer* **30** 1656–62
[33] Moloney A C, Kausch H H, Kaiser T and Beer H R 1987 Parameters determining the strength and toughness of particulate filled epoxide resins *J. Mater. Sci.* **22** 381–93
[34] Tron A, Hamid R, Zhang N, Paolella A, Wulfert-Holzmann P, Kolotygin V, López-Aranguren P and Beutl A 2023 Film processing of Li_6PS_5Cl electrolyte using different binders and their combinations *J. Energy Storage* **66** 107480
[35] Ruhl J, Riegger L M, Ghidiu M and Zeier W G 2021 Impact of solvent treatment of the superionic argyrodite Li_6PS_5Cl on solid-state battery performance *Adv. Energ. Sust. Res.* **2** 2000077